



HAL
open science

Quantification of soft soil cracking during suction cycles by image processing

R. Auvray, S. Rosin-Paumier, Adolf Abdallah, F. Masrouri

► **To cite this version:**

R. Auvray, S. Rosin-Paumier, Adolf Abdallah, F. Masrouri. Quantification of soft soil cracking during suction cycles by image processing. *European Journal of Environmental and Civil Engineering*, 2013, 18 (1), pp.11 - 32. 10.1080/19648189.2013.840250 . hal-01913250

HAL Id: hal-01913250

<https://hal.science/hal-01913250>

Submitted on 6 Nov 2018

HAL is a multi-disciplinary open access archive for the deposit and dissemination of scientific research documents, whether they are published or not. The documents may come from teaching and research institutions in France or abroad, or from public or private research centers.

L'archive ouverte pluridisciplinaire **HAL**, est destinée au dépôt et à la diffusion de documents scientifiques de niveau recherche, publiés ou non, émanant des établissements d'enseignement et de recherche français ou étrangers, des laboratoires publics ou privés.

Quantification of soft soil cracking during suction cycles by image processing

Auvray, R., Rosin-Paumier, S., Abdallah, A., Masrouri, F.

Romain.Auvray@Univ-Lorraine.fr

Sandrine.Rosin@Univ-Lorraine.fr

Adel.Abdallah@Univ-Lorraine.fr

Farimah.Masrouri@Univ-Lorraine.fr

LEMETA-UMR 7563 CNRS, Université de Lorraine, rue M. Roubault, 54501 Vandoeuvre-lès-Nancy, FRANCE.

ABSTRACT

Soil cracking has been studied for many decades; however, it still deserves further investigation. This paper describes a new testing device that uses image processing to perform simultaneous and continuous quantification of the vertical strain and radial strain, crack area, and water content of a soil specimen subjected to suction cycles imposed by the vapour equilibrium method. An image processing method was designed to determine the crack area and the soil radial strain separately. The evolution of each measured parameter over time in a clayey soil specimen subjected to 3 suction cycles is presented and discussed. The first suction cycle has the greatest impact on the crack area, the mass water content, the vertical strains and the radial strains. Hysteresis loops were observed for crack area and radial strain evolution.

Keywords : Soft Soil – Suction Cycles - Crack – Shrinkage - Image Processing.

1. Introduction

Soils with a significant proportion of swelling clays are very sensitive to variation in water content (Hillel, 1988). Swelling occurs when the water content increases, while shrinking occurs when the water content decreases. Non-uniform settlements in the soil under buildings and in soil subject to air desiccation can damage building foundations (e.g.,

27 Nelson and Miller., 1992; Maisa et al., 2004; Abdelmalak., 2007; Jahangir et al., 2011;
28 Jahangir et al. 2012). Moreover, drying increases tensile stresses that can locally exceed the
29 soil's tensile strength, which leads to the initiation of cracks (Konrad and Ayad, 1997). Cracks
30 can increase the hydraulic conductivity of soil by 1 to 3 orders of magnitude (Phifer et al.,
31 1994; Omid et al., 1995; Drumm et al., 1997; Miller et al., 1998; Yuen et al., 1998; Yesiller et
32 al., 2000; Albrecht et al., 2001; Tay et al., 2001, Rayhani et al., 2007; Sadek et al., 2007).
33 Cracks influence the swelling and shrinking of soils because they allow deeper layers to be
34 subjected to hydric variation. Cracks also decrease the bearing capacity of soil and constitute
35 points of weakness that may affect the stability and the integrity of geotechnical structures.
36 To prevent such effects, a better understanding of the swelling/shrinkage phenomenon and
37 the initialisation, propagation and impact of cracks on soil parameters is needed. To achieve
38 this objective, an accurate method for quantifying shrinkage and crack intensities under
39 suction-controlled conditions is needed.

40 Studies of volumetric shrinkage initiation and its effects on soil properties have
41 typically been conducted using uncracked soil samples. Under field conditions, some authors
42 have studied the relationship between the appearance of cracks and vertical volumetric
43 shrinkage (Kleppe and Olsen, 1981, Hewitt and Philip, 1999; Velde, 1999; Elias et al., 2001).
44 Kleppe and Olsen (1981) showed that cracks appear in a sand-bentonite mixture when its
45 volumetric shrinkage exceeds 10%. However, for some other soils, cracks may occur when
46 the volumetric shrinkage reaches 5% (Tay et al., 2001). A similar correlation was observed
47 under laboratory conditions, not only with vertical but also with horizontal shrinkage (Lloret et
48 al., 1998; Peng et al., 2006; Péron et al., 2009). Horizontal shrinkage typically occurs at the
49 interface between the soil and the cell wall. Some authors have studied the volumetric
50 changes of soil undergoing desiccation and have concluded that volumetric shrinkage
51 increases with increasing clay content and the initial water content (Bronswijk, 1991; Hallaire,
52 1991; Kleppe and Olsen, 1981; Tariq et al., 1993; Tay et al., 2001; Boivin et al., 2004).

53

54 Cracks change with climatic conditions and over time. Their depth and width increase
55 under intensively dry conditions, whereas during rainy periods, crack depth and width tend to
56 decrease, and cracks can close completely. This is known as the self-healing phenomenon
57 (Edgenbrod, 2003). Self-healing may not be complete in all cases, and can be limited to the
58 soil surface, which can potentially lead to water being trapped and pore pressure increasing
59 (Mallwitz, 1998). An important aspect of the study of soil cracking is quantifying crack pattern
60 characteristics to determine the influence of material properties, humidity and air temperature
61 on cracks. Some researchers have already identified some trends. Wider cracks and a
62 denser crack pattern were obtained for soils with a higher proportion of clay (Kleppe and
63 Olsen, 1985; Tay et al., 2001; Elias et al., 2001; Edgenbrod et al., 2003; Boivin et al., 2004;
64 Rayhani et al., 2007), a higher air temperature (Tang et al., 2010; Rayhani et al. 2007) and a
65 higher initial moisture content (Tay et al., 2001; Tang et al., 2010). Similarly, a higher initial
66 thickness of laboratory specimens resulted in more widely spaced cracks (Lloret et al., 1998;
67 Rodriguez et al., 2007; Atique and Sanchez, 2011).

68 Some image-based experimental devices have been developed to quantify, with
69 sufficient accuracy, crack development as a function of soil characteristics and environmental
70 conditions (Miller et al., 1998; Yesiller et al., 2000; Velde, 2001; Tay et al., 2001; Peng et al.,
71 2006; Lasmikantha et al., 2009; Tang et al., 2010; Atique and Sanchez 2011). These image-
72 based devices typically employ an image processing method to determine the crack intensity
73 factor (CIF) (Miller et al., 1998; Vogel et al., 2005; Peng et al., 2006, Larshmikantha et al.,
74 2009; Tang et al., 2010; Atique and Sanchez., 2011). The CIF was defined by Miller et al.
75 (1998) as the ratio between the crack area and the entire specimen surface area. The
76 evolution of the CIF was usually quantified using initially saturated soils subjected to air
77 drying or oven drying. These conditions lead to large cracks that are easily identifiable on the
78 specimen surface. However, air drying and oven drying do not allow control of the suction of
79 the specimen, defined as the water potential in a soil-vapour system (Richards, 1975), and
80 the saturated initial state may not be comparable to the natural state.

81 Cracking and shrinkage under laboratory conditions have been studied a great deal.
82 However, some researchers have combined the cracking surface and the shrinkage surface
83 into a single CIF value *referred to as* CIF_{tot} (Peng et al., 2006). Others have concentrated
84 their studies on cracks occurring on the inner surface of the specimen, leading to the
85 definition of another factor, referred to here as CIF^* (e.g., Miller et al., 1998; Yesiller et al.,
86 2000; Laskmikantha et al., 2009; Tang et al., 2010). As a result, methods are available to
87 quantify separately the crack surface or the shrinkage surface, but to our knowledge, no
88 automatic method has yet been proposed to quantify the two surfaces for the same sample.
89 This coupled quantification is needed to acquire a complete understanding of the influence of
90 drying on cracking.

91 The present study seeks to quantify the evolution of CIF and volumetric shrinkage in
92 a clayey specimen submitted to suction-controlled drying-wetting cycles at a constant
93 temperature of 20°C. The initial water content and dry density of the specimen were selected
94 within the range corresponding to a natural soil in a temperate climate. The material and the
95 experimental setup are presented in the first part of this paper. To quantify the cracks and
96 the shrinkage intensities in the specimen, an image processing method was developed and
97 is described in the second part of this paper. The method includes an algorithm to evaluate
98 the horizontal shrinkage. The image processing method was tested on calibrated real
99 images. The third part of this paper describes the application of the image processing
100 method to a sequence of 3,000 images obtained during the imposition of 3 successive
101 suction cycles to the specimen. The paper concludes with a discussion of the potential uses
102 of the image processing method developed and the impact of suction cycles on cracks and
103 shrinkage intensities in soils.

104

105

2. Materials and methods

106 A mixture of a bentonite and a natural silt from Xeuilley (in northeast France) was used in this
107 study. The mixture contains 40% Xeuilley silt and 60% bentonite by weight. The materials
108 were initially dried and sieved to 400 μm and then mixed together. The basic characteristics
109 of the materials and the mixture are summarised in Table 1.

110 2.1. Soil preparation

111 The soil was mixed with distilled water to reach a water content of 15.5% and cured for 24 h
112 under plastic wrap to homogenise the water content. The mixture was then sieved to 4 mm to
113 remove the largest aggregates. Such aggregates could influence desiccation by creating
114 preferential paths for drying in the inter-aggregate space, which in turn could influence the
115 development of cracking (Nowamooz and Masrouri, 2008). The measured water content
116 after sieving was 15.3%. The 20-mm-tall specimen was prepared, by static compaction, in
117 two layers in a stainless steel circular cell 102 mm in diameter and 60 mm in height to reach
118 a final dry density of 1.27 Mg/m^3 . The base of the cell is grooved to ensure good adhesion
119 between the soil and the cell.

120 2.2. Experimental setup

121 The specimen was placed in a hermetic container (Fig. 1) and exposed to 3 drying-wetting
122 cycles. These cycles were imposed using the vapour equilibrium method (Lide et al., 2002;
123 Blatz et al., 2008; ISO, 1999). This method consists of putting a specimen into a container
124 that includes a salt solution. The soil sample absorbs or desorbs water vapour until the
125 potential equilibrium is reached. The imposition of a given relative humidity (RH) on a soil
126 sample allows its suction to be controlled according to the Kelvin equation:

$$127 \quad s = -\gamma_w * \frac{RT}{Mg} \ln(RH) \quad [\text{Equation 1}]$$

128 where, s is pore negative air pressure or suction (kPa), R is universal constant for perfect
129 gases ($8.31 \text{ J}^{-1} \text{ mol}^{-1} \text{ K}^{-1}$), γ_w is the unit weight of water (9.81 kN m^{-3}), g is the gravitational
130 constant (9.8 m s^{-2}), M is molecular weight of water ($18 \cdot 10^{-3} \text{ kg mol}^{-1}$) and RH is relative
131 humidity (%). This method is influenced by a number of parameters, such as the type of salt
132 solution, pressure and temperature. Here to limit the influence of temperature, salts less
133 sensitive to temperature were selected.

134 The humidity and temperature in the container were measured continuously during the test to
135 control the applied suction. The suction target value is reached after a period of 5 to 24 hours
136 with 5% accuracy. The laboratory atmosphere was air-conditioned at 20°C .

137 During the test, the specimen was weighed continuously to measure the evolution of the
138 water content of the specimen. The specimen's height variations were measured with an
139 accuracy of 0.01 mm using a laser distance sensor fixed on a sliding pane. Nine
140 measurements, spaced at $10 \pm 0.01 \text{ mm}$, were taken every day along a diameter line of the
141 specimen.

142 To study the surface cracks and shrinkage of the specimen at the same time, a precise
143 camera positioned 350 mm from the surface of the specimen took photographs every 30
144 minutes. Because each cycle provides 1,000 images to be analysed, an automatic image
145 processing method is needed.

146 **2.3. Description of calibration images**

147 To test the performance of the different steps of image processing method allowing the
148 determination of the crack and the shrinkage intensities, two specimens images, named
149 images of calibrations, with inherent cracks are considered (Fig 2). Their crack and shrinkage
150 areas were calculated precisely. Calibration image n°1 (Fig. 2a) was obtained with the
151 experimental device; it corresponds to the image of the cracked surface of a specimen after
152 desiccation under a suction of 113 MPa for 21 days. This image shows large cracks and a

153 large shrinkage area. Calibration image n°2 (Fig. 2c) was obtained with the experimental
154 device and corresponds to the image of the cracked surface of a specimen after desiccation
155 under a suction of 113 MPa for 7 days. This image shows narrow cracks and a narrow
156 shrinkage area. The exact areas of the cracks and shrinkage were determined with *ImageJ*,
157 a public-domain software for image processing (Rosband 2006), by manually marking the
158 shrinkage area (S_{ref}) and the crack area (C_{ref}) using a method similar to the one used by
159 Peng et al. (2006) (fig. 2b). Peng et al. (2006) used the “magic wand” tool in *Adobe*
160 *Photoshop 7*, which separated cracks from the surface of the soil. In this study, the manual
161 determination of the cracks and shrinkage area was done using the “pencil” tool in *ImageJ*,
162 which allows the operator to manually fill the cracks or shrinkage areas. For calibration
163 images n°1 and n°2, respectively, this method yielded a shrinkage area (S_{ref1}) of 147 600 px
164 and a crack surface (C_{ref1}) of 34 565 px, and a shrinkage area (S_{ref2}) of 50 476 px and a crack
165 surface (C_{ref2}) of 16 273 px. This method is accurate but highly time-consuming and cannot
166 be used to process the 3,000 images captured during one test.

167 **3. Image processing method**

168 An automatic image processing method was developed to handle each image of a
169 test, to quantify the evolution of cracks and shrinkage areas in a specimen surface over time.
170 The method was programmed as an *ImageJ* plugin. This section presents the steps of the
171 image processing method, illustrated in the chart given in Fig. 3. To calibrate the method, the
172 image processing results for calibration images n°1 and n°2 were analysed and are
173 presented in section 3.3.3. The results from each step of the image processing method for
174 calibration image n°1 are given in Fig. 4. The implementation of this method in programmed
175 *ImageJ* plugins permitted automated processing of a sequence of 3,000 images, which is
176 presented and discussed in section 4.

177 **3.1. Preparation of the raw images**

178 The raw calibration image is an uncentred RGB (red green blue) image (Fig. 4a). The
179 preparation of the image for processing consists of converting the image to a greyscale
180 image and selecting the circular surface of the specimen to create a centred greyscale image
181 with a white background. This is referred to as the prepared image (Fig. 4b). The contour line
182 of the specimen surface is referred to as C_{ext} . It was determined manually for the first image
183 and then computed in the plugin. The RGB image is converted in gray-scale image by using
184 a method proposed by Lakshmikantha et al. (2009).

185 **3.2. Filtering of the prepared image**

186 The prepared image preserves the defaults of the raw image, such as the uneven
187 illumination of the specimen's surface and texture artefacts. To correct the image
188 illumination, some authors such as Lakshmikantha et al. (2009) have used an *ImageJ*
189 function called *subtract background*. This tool removes smooth continuous backgrounds
190 using a rolling ball algorithm (Sternberg, 1983). The rolling ball radius has to be at least as
191 large as the radius of the largest object in the image that is not a part of the background.
192 However, the area of the elements of the cracks or the shrinkage surface changes over time
193 during the test. Moreover, the size of the cracks and the size of the elements of the
194 shrinkage area are quite different, and this difference also changes during the drying and
195 wetting stages. These two facts make the definition of the required rolling ball radius for each
196 image quite impossible.

197 To correct the uneven illumination and the deformation of the specimen during the drying,
198 Vogel et al. (2005) used a local threshold and compare the crack detection of the successive
199 images. Base on this concept, the surface of our prepared image was filter by a reference
200 filter. The reference filter is applied to each prepared image of the sequence by addition. The
201 resulting image, referred to as the corrected image (Fig. 4c), represents only the difference
202 between the initial specimen surface image and the current specimen image. Consequently,
203 the uneven illumination of the specimen is corrected assuming constant lighting during the

204 test. This method can be applied to images without consideration of their scale, size, shape
205 and the nature of the soil. The reference filter is prepared manually before the image analysis
206 process begins and must be changed for each test.

207 Because the aim of the image processing method is to determine the shrinkage area and the
208 inner crack area independently, the image processing method was then divided into two
209 parts. The first part determines the shrinkage area and the second part determines the inner
210 crack area.

211 **3.3. Determination of the shrinkage area**

212 *3.3.1. Segmentation of the corrected image*

213 The corrected image is a greyscale image. To differentiate the cracks and the shrinkage area
214 from intact soil, an image segmentation is needed. The segmentation divides the digital
215 image into multiple regions, according to a chosen criterion, for example, a threshold. In this
216 study, the threshold is the greyscale value that defines the limit between the cracks and the
217 shrinkage area (the darker pixels), and the intact soil (the brighter pixels). The segmentation
218 consists of comparing each pixel of the greyscale image to the threshold. If the pixel is darker
219 than the threshold, its value becomes 0 (a black pixel); otherwise, its value becomes 255 (a
220 spurious white pixel). As a result, the corrected image becomes a binary image, called a
221 segmented image (Fig. 4d). The choice of the final threshold *ImageJ* function used to
222 determine the shrinkage area is described in section 3.3.3. The choice is based on a
223 comparison of the results obtained from the complete image processing method with
224 different threshold functions applied to the calibration images.

225 After the segmentation, some white points appear in the shrinkage area and may lead to an
226 underestimation of its surface area. Some binary operators can improve the accuracy by
227 filling these white points (Serra, 1982). The *Dilate* operator switches a pixel black if all of the
228 pixels nearby are black, whereas the *Erode* operator switches a pixel to white if all of the
229 pixels nearby are white. The *Close* operator is a combination of the *Dilate* operator and the

230 *Erode* operator. This operator makes it possible to fill the holes in the shrinkage area.
231 Various combinations of binary operators such as *Erode*, *Dilate*, *Open* and *Close* were tested
232 on the calibration images to fill the white points present in the shrinkage area. The *Close*
233 operator succeeded in improving the shrinkage area quantification. After the application of
234 the binary operator *Close*, the segmented image results in the final image (Fig. 4e).

235 3.3.2. Application of the Diameter algorithm

236 To determine the shrinkage area, an *ImageJ* plugin was developed in JavaScript during this
237 study. This algorithm, called the “diameter algorithm”, seeks to determine the area between
238 the cell wall and the border of the specimen. The specimen border is difficult to determine
239 because it changes with the swelling or shrinkage of the specimen. The diameter algorithm
240 considers several diameter lines spaced one degree apart. Each diameter intersects the cell
241 at two points, A_c and B_c , and the border of the specimen at another two points, A_s and B_s
242 (Fig. 5). The shrinkage area corresponds to the number of pixels between A_c and A_s and
243 between B_c and B_s . The algorithm counts the number of black pixels starting at A_c until it
244 encounters 5 consecutive white pixels. As a result, the black pixels corresponding to the
245 cracks are not counted. This value of 5 pixels allows the algorithm to keep counting even if
246 white points are still present in the shrinkage surface. Because the specimen radial
247 deformation may not be perfectly axisymmetric, a sufficient number of diameters have to be
248 determined. Fig. 6 shows the evolution of the relative error between the shrinkage area
249 calculated with the diameter algorithm and the S_{ref} according to the number of diameters
250 considered. The curve shows that considering at least 180 diameters leads to an accurate
251 determination of the shrinkage area. The higher the number of diameters considered, the
252 more accurate and the more time-consuming the calculation. As a consequence, 180 was
253 chosen as the number of diameters needed.

254 The shrinkage area was then determined, presuming that the shrinkage is constant along an
255 arc of a circle of 0.5 degrees around each extremity of the diameter. The mean values of the

256 radial shrinkage as well as the maximum value of the horizontal shrinkage are also
257 determined. Given the value of radial shrinkage, the value of the radial strains can be
258 calculated from the diameter algorithm.

259 3.3.3. Choice of the threshold function

260 Various threshold functions are implemented in *ImageJ* and are easily accessible through the
261 *ImageJ* Interface (see Table 2). In the following section, we present the selection of the
262 function for threshold determination.

263 3.3.3.1. Determination of the threshold function

264 Because the image processing method seeks to quantify the shrinkage area and cracks of a
265 specimen, it has to be efficient for both large and small cracks and shrinkage areas. The
266 quantification of a large shrinkage area is easier because the pixels corresponding to a large
267 area are darker and more numerous than those corresponding to a smaller area. The pixels
268 of a large shrinkage area have a greater influence on the greyscale histogram, which results
269 in easier determination of the threshold value. As a consequence, a threshold function that is
270 efficient in quantifying a large shrinkage area might not be accurate enough to quantify a
271 small shrinkage area.

272 On the basis of these observations, a two-step method for choosing the threshold *ImageJ*
273 function was defined. The first step consisted of applying different threshold *ImageJ* functions
274 to calibrate image n°1, which contains quite large cracks and a large shrinkage area (Fig.
275 2a). A comparison of the different results with the manually determined values, S_{ref1} , is
276 presented in section 2.3. The *ImageJ* threshold functions that yielded a value for the
277 shrinkage area close to 10% of S_{ref1} were selected. The second step consisted of applying
278 the selected threshold *ImageJ* function to calibrate image n°2, which contains quite small
279 cracks and a small shrinkage area (Fig. 2c). A comparison of the different results with the
280 manually determined values, S_{ref2} , is presented in section 3.3.

281 3.3.3.2. Results

282 Table 3 presents the shrinkage areas and their relative error obtained using different *ImageJ*
283 threshold functions for calibration image n°1. The results are compared to S_{ref1} . The results
284 for the *Li*, *MinError* and *Shanbag* threshold *ImageJ* functions are not presented in Table 3
285 because they were not able to detect shrinkage elements. The low contrast of the corrected
286 image (Fig. 4c) made the use of the *Triangle*, *Huang*, *Intermodes*, *Mean*, *Minimum* and
287 *Percentile* threshold *ImageJ* functions inefficient. Other threshold *ImageJ* functions, namely
288 *Otsu*, *IsoData*, *IJ_isodata*, *Moment*, *Max_Entropy*, *Yen* and *RenyiEntropy*, yielded an
289 accurate estimation of the shrinkage area for calibration image n°1. These threshold *ImageJ*
290 functions were then applied to calibration image n°2 (Table 4). The *Otsu*, *IsoData*, *IJ_isodata*
291 and *Moment* threshold *ImageJ* functions yielded an inaccurate quantification of the shrinkage
292 for calibration image n°2. Thus, these functions were not chosen. The 3 remaining threshold
293 *ImageJ* functions, named *Yen*, *RenyiEntropy* and *Max_Entropy*, yielded correct estimations
294 of the shrinkage area for both calibration images. These 3 functions have the same basis: an
295 element is detected if its greyscale level presents a large difference from those of
296 neighbouring elements. These functions also provide the same accuracy (Table 2, Table 3).
297 We present herein the results obtained with the *Max_Entropy* function.

298 3.4. Determination of the crack area

299 To improve crack detection, a ring with a width equal to the maximum value of horizontal
300 shrinkage was deleted from the corrected image (Fig. 4c) to remove the entire shrinkage
301 area. The resulting image is called the reduced corrected image (Fig. 4f). The efficiency of
302 the different threshold *ImageJ* functions was compared to C_{ref1} and C_{ref2} , which are the values
303 of the crack area for calibration images n°1 and n°2, respectively, determined as described in
304 section 2.3. The *Max_Entropy* function was selected and applied to the reduced corrected
305 image (Fig. 4g). Lakmikantha et al. (2009) proposed the use of a *Despeckle* median filter that
306 replaces each pixel with the median value (white or black) of the pixels in its immediate

307 vicinity. This filter is considered to be efficient in reducing the noise in binary pictures.
308 Therefore, a combination of the *Despeckle* median filter and the *Close* operator was applied
309 to the image to delete elements of the remaining noise and to fill crack elements (Fig. 4h).

310 The *analyze particle* command was then used to calculate the number of black pixels in the
311 reduced binary image, which corresponds to the crack area.

312 This value is computed and divided by the area of the reduced specimen to obtain CIF^*
313 (Equation 5). The sum of the crack area and the shrinkage area is divided by the initial
314 specimen area to determine the CIF_{tot} (Equation 6).

$$315 \quad CIF^* = \frac{Crack\ area}{Reduced\ specimen\ area} * 100 \quad [Equation\ 5]$$

$$316 \quad CIF_{tot} = \frac{Crack\ area + Shrinkage\ area}{Initial\ specimen\ area} * 100 \quad [Equation\ 6]$$

317

318 **4. Application of the procedure to a complete test**

319 The calibrated image processing method was applied to a complete drying/wetting test of the
320 previously described silt-bentonite specimen. The test included 3 suction cycles ranging from
321 20.5 MPa to 113 MPa, corresponding to air relative humidities of 86% and 46%, respectively.
322 Each cycle comprises one drying phase and one wetting phase. Fig. 7a illustrates the
323 evolution of the imposed suction over time and shows that the water content reaches
324 equilibrium almost 20 days after the imposition of suction.

325 **4.1. Hysteresis and evolution of measured parameters**

326 Fig. 7b and 7c present the evolution of the mass water content and vertical strain,
327 respectively, with time, and Fig. 8 shows the evolution of the vertical strain with mass water
328 content. The vertical strain value is calculated using the height of the specimen obtained by
329 averaging the nine measurements obtained by the laser sensor. The first drying **phase**

330 appears to have the greatest influence because the variation of the different parameters is
331 more significant during the first drying stage than during the later drying stages. The first
332 drying/wetting cycle showed, for imposed suctions of similar magnitude, significant hysteresis
333 of the water content (from 15.3% to 10.5%) and of the vertical strains (from 0 to 1%). No
334 more irreversible variation could be observed at the end of several subsequent cycles.
335 Indeed, the soil seems to exhibit elastic reversible behaviour after the first drying/wetting
336 cycle associated with the reduction of the range of water content variation and the
337 development of unrecoverable vertical deformation (Fig. 8).

338 **4.2. Description of crack patterns**

339 The figure 9 presents the surface specimen at different moment of the first phase of drying.
340 To improve the specimen cracks observation the contrast of figure 9b to 9h was increased.
341 Early in the first drying phase, numerous tiny cracks appear homogeneously distributed on
342 the soil surface (Fig. 9a, 9b, 9c, 9d). With further desiccation, some of these cracks grow in a
343 preferential manner, whereas others tend to close (Fig. 9e, 9f, 9g, 9h). The remaining
344 observed cracks have a radial orientation, and their angles of intersection are 90°, 60° and
345 120°. Radial shrinkage can be observed to occur simultaneously with the growth of the
346 main cracks.

347 Fig. 10 presents images of the specimen surface at successive wetting/drying phases (Fig.
348 10a corresponds to Fig. 9a, and Fig. 10b corresponds to Fig. 9h). After the first wetting
349 phase, partial self-healing occurs, and some of the main cracks remain open (Fig. 9). During
350 the next drying phase, the remaining unclosed cracks form preferential desiccation zones
351 from which cracking propagates, following the previous pattern, and no new cracks appear
352 (Fig. 10d). Subsequent wetting/drying cycles produce the same trends (Fig. 10f).

353 **4.3. Radial shrinkage and CIF evolution**

354 The image processing method was applied to the images of the previously presented test to
355 estimate the radial strains during the cycles (Fig. 11, Fig. 12). This facilitated the comparison
356 of the evolution of the shrinkage area and the inner crack area (Fig. 13). The amplitude of the
357 shrinking area appears to be of the same order of magnitude as the inner crack area and
358 appears to follow a similar evolution. Significant hysteresis was observed after the first

359 drying-wetting cycle, while a reversible trend was noticed during the second and the third
360 cycles.

361 The evolution of the radial strains and the CIF* versus the vertical strain are shown in Fig.
362 14a and Fig. 14b, respectively. The evolution of the two parameters is similar. Indeed,
363 neither shrinking nor cracking is observed until the vertical strain reaches a value of 0.3%.
364 The evolution is then very slow and quasi-linear until the vertical strain reaches a value of
365 0.6%. Then, the variation becomes sharper. After subsequent drying/wetting cycles, the
366 irreversible (plastic) radial strain reaches 1%. A difference between the wetting path and the
367 drying path is clearly observed for the two parameters, forming hysteresis loops, although
368 these loops are narrower for the radial strain than they are for the CIF*. For the first drying
369 phase the CIF* seems to be links with radial stains by a linear relation (fig. 14c) and. the
370 cracks and the radial stains seems to initiate in the same time. A difference is observed in
371 the drying and wetting paths for the different cycles. The drying path of the second and the
372 third cycle (respectively the wetting phase) are the same.

373 **5. DISCUSSION**

374 Using the method described in this paper, the influence of suction cycles on cracking in soils
375 has been studied with an accuracy of within 5% with respect to the results obtained for
376 calibration images. Suction was the only parameter that was varied; the temperature was
377 held constant. This point is particularly important because no previous studies have imposed
378 suction-controlled cycles on soil specimens while monitoring the evolution of cracks. The
379 image processing tool described in this paper makes it possible to determine the evolution of
380 both the radial strain and the crack area over time with changes in suction.

381 **5.1. Volumetric strains**

382 Alonso et al. (2005) studied the impact of suction cycles, from 4 MPa to 120 MPa, on clayey
383 silt at a water content of 10.5% (a degree of saturation of 37%) on an uncracked specimen.
384 Samples were subjected to various vertical net stresses (92 kPa, 196 kPa and 396 kPa).

385 Their results showed an accumulation of shrinkage strain with the number of cycles and a
386 convergence of the vertical strain towards a reversible state. Nowamooz and Masrouri
387 (2008) studied the evolution of vertical strain in a soil specimen subjected to wetting and
388 drying suction cycles between 0 and 2 MPa. The tested samples showed cumulative swelling
389 strains during the cycles, which finally converged towards an equilibrium stage. All of the
390 tests exhibited completely reversible behaviour after 2 to 3 suction cycles.

391 In this study, the strains also converged to a reversible state after an influential first drying
392 phase. Indeed, there was a 5% decrease between the vertical strains at the end of the first
393 drying phase and at the end of the third drying phase, whereas the radial strains after the
394 third cycle were 5% higher than the radial strains after the first cycle. It seems that the
395 presence of cracks did not influence the relationship between the vertical strains and the
396 suction cycle.

397 **5.2. CIF^* and CIF_{tot}**

398 Another unique aspect of this study was the use of an image processing method to
399 determine the radial strains, which made it possible to distinguish between crack area and
400 shrinkage area. In previous studies (Miller et al. 1998; Yesiller et al. 2000, Tang et al. 2008,
401 2009, 2011), the shrinkage area was eliminated to limit the CIF determination to the inner
402 part of the specimen ($CIF=CIF^*$). However, the evolution of the radial strains is also
403 interesting because it may contribute to a better understanding of the cracking phenomenon.

404 As observed in section 4.1, the evolution of the CIF^* and the CIF_{tot} became reversible after
405 the first cycle (Fig. 13). For each phase, the CIF^* (and CIF_{tot}) changed sharply when suction
406 was first imposed; then, the evolution became more gradual, until it converged towards an
407 equilibrium state. The value of CIF^* (and CIF_{tot}) at the end of the wetting phase (drying
408 phase) did not change with the number of cycles.

409 Tang et al. (2008) reported a decrease of the CIF^* with an increasing number of
410 wetting/drying cycles. Their study concerned the impact of very intense drying/wetting cycles

411 on an initially saturated slurry. The cycles imposed included an oven drying phase (between
412 30°C and 50°C), and a direct imbibition phase. In their study, the initial unconsolidated state
413 and the high water content of the soil slurry could explain the high CIF* value obtained during
414 the first drying phase. During the subsequent cycles, soil densification, which could not be
415 quantified during their tests, might have been responsible for the decrease in the CIF*. The
416 simultaneous measurement of each geometric parameter is needed to explain the sample
417 evolution.

418 On the contrary, Yesiller et al. (2000) and Tay et al. (2001) demonstrated an increasing CIF*
419 with an increasing number of wetting/drying cycles. However, it should be noted that they
420 tested large surface-compacted specimens (800 mm to 1500 mm in width and 200 mm to
421 500 mm in depth). The wetting phase was imposed by watering the soil surface, which may
422 have led to local moisture gradients. Desiccation was achieved by air drying coupled with
423 ventilation at the soil surface, which may have induced non-uniform drying. These results
424 suggest that intense and non-uniform wetting/drying cycles favour preferential crack initiation
425 and lead to the creation of dense crack patterns (a 5% CIF* value was obtained by Yesiller et
426 al., 2000). Moreover, the crack pattern observed by Tay et al. (2001) was influenced by the
427 compaction procedure (a pneumatic hammer attached to a vibrating plate); they noted that
428 some of the cracks followed the surface depression caused by the compaction equipment.

429 In this study, the stabilisation of CIF* values observed after the first cycle may be explained
430 on the one hand by the static compaction of the soil specimen, which avoided the formation
431 of weak zones and preferential crack initiation and propagation, and on the other hand by the
432 suction-controlled test process, which permitted gradual and uniform wetting/drying
433 conditions at the soil surface. However, more results are needed to confirm this observation.

434 **5.3. Hysteresis loops**

435 The evolution of the vertical strains, radial strains, CIF^* and CIF_{tot} with respect to the water
436 content showed hysteresis loops. Indeed, for a given cycle, the wetting and drying curves
437 were not identical for any of the parameters studied.

438 The hysteresis loops corresponding to the vertical and radial strains are narrow (Fig. 8, 12),
439 whereas the CIF^* loops are large (Fig. 15). Moreover, the comparison of the evolution of
440 CIF_{tot} and CIF^* with the mass water content (Fig. 15) showed that the main part of the
441 hysteresis loops were linked to the inner crack formation. The difference between these two
442 curves mainly corresponded to the plastic volumetric deformation accumulated during the
443 first drying phase.

444 The hysteresis loops were also observed in continuous media in previous studies that were
445 focused on the evolution of volumetric strain with the number of suction cycles (Alonso et al.,
446 2005; Nowamooz and Masrouri, 2008). After Gens and Alonso (1992), in an expansive soil,
447 these loops for volumetric strains are in large part due to the two structural levels in the
448 fabric: micro and macro-structure. During the first drying phase, with the loss of water content
449 and the increase of suction, a rearrangement of the macro-structure appears which induces
450 a densification of the specimen with decreasing the volume of the large pores and inducing a
451 decrease of the mean height and the diameter of the specimen. These strains are in a large
452 part irreversible due to the hysteresis effect which could be attributed to: geometric
453 nonuniformity of individual pores, resulting from the "Ink Bottle" effect; different spatial
454 conductivity during drying and wetting process, variation in liquid-solid contact angle; and air
455 entrapment (Hillel, 1980; O'Kane, Pokrovskii, & Flynn, 2004). For instance, the hysteresis
456 loops in cracked specimen could be explained in the same manner as in continuous
457 samples. Further investigations are needed to confirm this hypothesis..

458 **5. CONCLUSIONS**

459 In this paper, a device for studying the evolution of soil specimens subjected to controlled
460 wetting/drying cycles was presented. The device, coupled with an image processing method,

461 allows the simultaneous measurement of the evolution of various soil parameters, such as
462 the water content, the vertical strains, the radial strains, and the crack area evolution over
463 time. This device and the associated image processing software make it possible to study
464 the evolution of these parameters during wetting and drying cycles applied by varying the
465 suction, rather than just the evolution of the equilibrium value of the parameters at the end of
466 each wetting and drying phase. 3 suction cycles were applied to a circular test specimen
467 composed of a mixture of bentonite and silt in this study. The following observations were
468 made:

- 469 - All parameters exhibited hysteresis loops.
- 470 - The first cycle was the most influential.
- 471 - All of the studied parameters converged towards a reversible state as the number of
472 suction cycles increased.

473 During the various tests involved in the development of the procedure, circular specimens of
474 different sizes were successfully tested, and the image processing was able to determine the
475 evolution of cracks over time. This procedure can be used in a laboratory environment
476 without it being necessary to take into account the laboratory lighting system. As a
477 consequence, the impact of varying suction intensity on a cracked soil surface, as well as the
478 impact of the initial state of the specimen (water content after compaction, clay content and
479 dry density) can also be studied. This can lead to a better understanding of the relation
480 between suction and cracking in soft soils.

481 **Acknowledgements**

482 The authors thank M. R. Caël for his technical assistance with electronics and test
483 conception, and M. C. Morlot and M. E. Lefevre for their technical assistance with
484 photography issues.

485

486 **References**

- 487 Abdelmalak, R. 2007. Soil structure interaction for shrink-swell soils. A new design procedure
488 for foundation slabs on shrink-swell soils. Ph.D. Thesis, Texas A&M. University.
- 489 Albrecht, B., Benson, C., Members, 2001. Effect of Desiccation on Compacted Natural Clays.
490 Journal of Geotechnical & Geoenvironmental Engineering 127 (1), 67-75.
- 491 Alonso, E.E., Romero, E., Hoffemann, C, Garía-Escudero,E., 2005. Expansive
492 bentonite/sand mixtures in cyclic controlled suction drying and wetting. Engineering Geology
493 81, 213-226.
- 494 ASTM, 1998. Standard test Method for Liquid Limit, Plastic Limit, and Plasticity Index of
495 Soils. In annual Book of ASTM standards vol. 04.08, 519-529, American Society for Testing
496 Materials, Designation D4318-98.
- 497 ASTM, 2006. Standard test Method for Specific Gravity of Soil Solids by Gas Pycnometer. In
498 annual Book of ASTM standards vol. 15.02. American Society for Testing Materials,
499 Designation D5550-06.
- 500 ASTM, 2009. Standard Test Method for Methylene Blue Index of Clay. In annual Book of
501 ASTM standards vol. 15.02. American Society for Testing Materials, Designation C837-09.
- 502 Atique, A., Sanchez, M., 2011. Analysis of cracking behavior of drying soil. 2nd International
503 Conference on Environmental Science and Technology IPCBEE 6, IACSIT Press Singapore
504 vol 1, 66-70
- 505 Blatz, J.A., Cui, Y-J., Oldecop, L., 2008. Vapour equilibrium and osmotic technique for suction
506 control . Geotechnique Geotechnical Engineering 26, 661-673.
- 507 Boivin, P., Garnier, P., Tessier, D., 2004. Relationship between clay content, clay type, and
508 shrinkage properties of soil samples. Soil Science Society of America Journal 68, 1145-1153.
- 509 Bronswijk, J., 1991. Relation between vertical soil movements and water-content changes in
510 cracking clays, Soil Science Society of America Journal 55, 1220-1226.
- 511 Doyle, W., 1962. Operation useful for similarity-invariant pattern recognition. Journal of the
512 Association for Computing Machinery 9, 259-267.
- 513 Drumm, E. C., Boles, D.R., Wilson, G., V., 1997. Desiccation cracks result in preferential
514 flow. Environmental Geotechnics 15(2), 22-25
- 515 Eigendbrod, K.D., 2003. Self-healing in fractured fine-grained soils. Canadian Geotechnical
516 Journal 40, 435-449.
- 517 Elias, E., Salih, A., Alaily, F., 2001. Cracking patterns in the Vertisols of the Sudens Gezira at
518 the end of dry season. International Agrophycs 15(3), 151-155.
- 519 Gens, A., Alonso, E.E., 1992. A framework for the behaviour of unsaturated expansive clays.
520 Canadian Geotechnical Journal 29, 1013-1032.
- 521 Glasbey, C.A., 1993. An analysis of histogram-based thresholding algorithms. CVGIP:
522 Graphical Models and Image Processing 55, 532-537.

523 Hallaire, V., 1991. Une méthode d'analyse bidimensionnelle du retrait d'échantillons naturels
524 de sol. *Science Du Sol* 29(2), 147-158.

525 Hewitt, P.J., Philip, L.K., 1999. Problems of clay desiccation in composite lining systems.
526 *Engineering Geology* 53, 107-113.

527 Hillel, D. (1980). *Fundamentals of soil physics* (p. 413). New York, NY: Academic Press.

528 Hillel, D., 1988. *L'eau et les sols, principes et processus physiques* Louvain-la-Neuve:
529 Academia. ISBN: 2-87209-015-0. Collection PEDASP.287p

530 Huang, L-K., Wang, M.J J., 1995. Image thresholding by minimizing the measure of
531 fuzziness. *Pattern Recognition* 28(1), 41-51

532 ISO, 1999. ISO 483 : Petites enceintes de conditionnement et d'essai utilisant des solutions
533 aqueuses pour maintenir l'humidité relative à une valeur constante. International
534 Organisation for Standardization, 11p

535 Jahangir, E., Deck, O., Masroui, F., 2011. Influence of foundation embedding on clays
536 shrinkage-swelling hazard consequences. 3rd International Symposium on Geotechnical
537 Safety and Risk, Munich, Germany 2011, 117-124.

538 Jahangir, E., Deck, O., Masroui, F., 2012. Estimation of the ground settlement beneath
539 foundations due to shrinkage of clayey soils. *Canadian Geotechnical Journal* 49(7), 835-852

540 Kapur, J., Sahoo, P., Wong, A., 1985. A new method for graylevel picture thresholding usig
541 the entropy of the histogram. *Computer Graphics and Image Processing* 29(3), 273-285.

542 Kittler, J., Illingworth, J., 1986. Minimum error thresholding. *Pattern Recognition* 19,
543 41-47

544 Konrad, J.-M., Ayad, R., 1997. An Idealized Framework for the Analysis of Cohesive Soils
545 Undergoing Desiccation. *Canadian Geotechnical Journal* 34, 477-488.

546 Kleppe, J.H., Olson, R.E., 1985. Desiccation cracking of soil barrier. *Hydraulic Barrier in Soil
547 and Rock*, ASTM STP 874, A.I.Johnson, R.K. Fobel, N.J. Cavali, and C.B. Petterson, Eds.,
548 American Society for Testing and Materials, Philadelphia, 1985, 263-275.

549 Lakshmikantha, M, Prat, P., Ledesma, A., 2009. Image Analysis for the quantification of a
550 developing crack network on a drying soil. *Geotechnical Testing Journal* 32 (6), 505-515.

551 Li, C.H., Lee, C.K.,1993. Minimum Cross Entropy Thresholding. *Pattern Recognition* 26(4),
552 617-625.

553 Li, C.H., Tam, P.K.S.,1998. An Iterative Algorithm for Minimum Cross Entropy Thresholding.
554 *Pattern Recognition Letters* 18(8), 771-776.

555 Lide, D.R., 2002. *Handbook of chemistry and physics*. 82nd edition, CRC press, 15.25-15.26.

556 Lloret, A., Ledesma, A., Rodriguez, R., Sanchez, M., Olivella, S., Suriol, J, 1998. Crack
557 initiation in drying soils. *Proceedings of the Second International Conference on Unsaturated
558 Soils*, Beijing China, International Academic Publisher, 497-502.

559 Maisa M.J., Kleeman P.W., Melchers R.E. (2004). Soil/structure interaction modelling of
560 masonry for reliability studies. *Journal of structural Engineering* 130, 641-649.

561 Malawitz, K., 1998. Crack-healing in damaged compacted clay liners in waste deposits. In
562 Proceedings of the 3rd International Congress on Environmental Geotechnics, Lisbon,
563 Portugal, 7-11 September, 347-352.

564 Miller, C.J., Mi, H., Yesiller, N., 1998. Experimental Analysis of Desiccation Crack Propagation
565 in Clay Liners. *Journal of the American Water Resources Association* 34 (3), 677-686.

566 Nelson, J.D., Miller, D.J., 1992. Expansive soils: problems and practice in foundation and
567 pavement engineering. John Wiley & Sons Ltd., New York. 259 pages.

568 Nowamooz, H., Masrouri, F., 2008. Hydromechanical behavior of an expansive bentonite/silt
569 mixture in cyclic suction-controlled drying and wetting tests. *Engineering Geology* 101 (3-4)
570 154-164.

571 Nowamooz, H., Masrouri, F., 2010. Influence of suction cycles on the soil fabric of
572 compacted swelling soil. *Comptes Rendus Geosciences* 342 (1), 901-910.

573 O’Kane, J. P., Pokrovskii, A., & Flynn, D. (2004). The best model for testing the importance of
574 hysteresis in hydrology. *Proceedings of EGU conference*, vol. 6, 07303.

575 Omid, G.H., Thomas, J.C., Brown, K.W., 1996. Effect of desiccation cracking on the
576 hydraulic conductivity of a compacted clay liner, *Water Air and Soil Pollution* 89 (1-2), 91-
577 103.

578 Otsu, N., 1979. A threshold selection method from gray-level histograms, *IEEE Trans*
579 *System, Man and Cybernetics Society* 9(1), 62-66.

580 Peng, X., Horn, R., Peth, S., Smucker, A., 2006. Quantification of soil shrinkage in 2D by
581 digital image processing of soil surface. *Soil & Tillage Research* 91, 173-180.

582 Peron, H., Hueckel, T., Laloui, L., Hu, L., 2009. Fundamentals of desiccation cracking of fine-
583 grained soils : experimental characterisation and mechanisms identification 46, 1177-1201.

584 Phifer, M., Boles, D., Drumm, E., Wilson, G.V., 1995. Comparative response of two barrier
585 soils to post compaction water content variations. *ASCE GSP* 46, 591-608.

586 Prewitt, J.M.S., Mendelsohn, M.L., 1966. The analysis of cell images. *Annals of the New York*
587 *Academy of Sciences* 128, 1035-1053.

588 Rasband, W.S., 2006. “ImageJ”, National Institute of health, <http://rsb.info.nih.gov/ij/>

589 Rayhani, M.H.T., Yanful, E.K., Fakher, A., 2007. Desiccation-induced cracking and its effect
590 on the hydraulic conductivity of clayey soils from Iran. *Revue Canadienne de Géotechnique*
591 44, 276-283.

592 Richards, B.G., 1974. Behaviour of unsaturated soils. *Soils Mechanics-new horizons*,
593 American Elsevier, New York, 112-157.

594 Ridler, T.W., Calvard, S., 1978. Picture thresholding using an iterative selection method, IEEE
595 Transactions on Systems, Man and Cybernetics 8, 630-632

596 Rodriguez, R., Sánchez, M., Ledesma, A., Lloret, A., 2007. Experimental and numerical
597 analysis of desiccation of a mining waste. Canadian Geotechnical Journal 44(6), 644-658.

598 Sadek, S., Ghanimeh, S., El-Fadel, M., 2007. Predicted performance of clay-barrier landfill
599 covers in arid and semi-arid environments. Waste Management 27, 572-583.

600 Serra, J., 1982. Image Analysis and Mathematical Morphology, Academic Press, London.

601 Shanbhag, A.G., 1994. Utilization of information measure as a means of image thresholding,
602 Graph. Models Image Process. (Academic Press, Inc.) 56 (5), 414-419.

603 Sternberg, S., 1983. Biomedical Image Processing. Computer 16 (1), 22-34.

604 Tang, C., Shi, B., Liu, C., Zhao, L., Wang, B., 2008. Influencing factors of geometrical
605 structure of surface shrinkage cracks in clayey soils. Engineering Geology 101, 204-217.

606 Tang, C.S., Cui, Y.J., Tang, A.M., Shi, B., 2010. Experimental Evidence on the Temperature
607 Dependence of Desiccation cracking behavior of Clayey soil. Engineering Geology, 114,
608 261-266.

609 Tang, C.S., Cui, Y.J., Shi, B., Tang, A.M., Liu, C., 2011. Desiccation and cracking behaviour
610 of clay layer from slurry state under wetting-drying cycles. Geoderma 166(1), 111-118.

611 Tariq, A., Durnford, D., 2001. Shrinkage and desiccation cracking in bentonite-sand landfill
612 liners. Engineering Geology 60, 263-274.

613 Tay, Y., Stewart, D., Cousens, T., 2001. Shrinkage and desiccation cracking in bentonite-
614 sand landfill liners. Engineering Geology 60, 263-274.

615 Tsai, W., 1985. Moment-preserving thresholding: a new approach., Computer Vision,
616 Graphics, and Image Processing 29, 377-393.

617 Velde, B., 1999. Structure of Surface Cracks in Soil Muds. Geoderma 93, 101-124.

618 Velde, B., 2001. Surface Cracking and Aggregate Formation Observed in a Renzina Soil.
619 Geoderma 99, 203-211.

620 Vogel, H., Hoffmann, H., Roth, K., 2005. Studies of Crack Dynamics in Clay Soil I:
621 Experimental Methods, Results and Morphological Quantification. Geoderma 125, 203-211.

622 Yen, J.C., Chang S., 1995. A New Criterion for Automatic Multilevel Thresholding. IEEE
623 Trans. On Image Processing 4(3), 370-378.

624 Yesiller, N., Miller, C., INCI, G., Yaldo, K., 2000. Desiccation and cracking behavior of three
625 compacted landfill liners soils. Engineering Geological 57, 105-121.

626 Yuen, K., Graham, J., Janzen, P., 1998. Weathering induced fissuring and hydraulic
627 conductivity in natural plastic clay. Canadian Geotechnical Journal 35 (6), 1101-1108.

628 Zack, G.W., Rogers, W.E., Latt, S.A., 1977. Automatic measurement of sister chromatid
629 exchange frequency. *Journal of Histochemistry & Cytochemistry* 25 (7), 741–753.
630

631 Table 1: Main characteristics of the materials

	Norme	Xeuilley silt	Bentonite	40/60Mixture
Liquid limit (%)	ASTM,1993	36.8	117	82.2
Plastic limit (%)	ASTM, 1993	27.6	41.2	29.6
Plasticity Index (%)	ASTM, 1993	9.2	75.8	52.6
MVB (mg/g) (Sahin et al., 2013)	ASTM, 2009	31.3	184.1	115.3
Specific density (g/cm³)	ASTM, 2006	2.65	2.55	2.58

632

633 Table 2. Threshold algorithm *ImageJ* functions

Algorithm threshold ImageJ function	References
Huang	Huang and Wrang, (1995)
Intermodes	Prewitt and Mendelsohn, (1966)
IsoData	Ridler and Calvard, (1978)
Li	Li and Lee, (1993, 1998)
MaxEntropy	Kapur et al., (1985)
Mean	Glasbey (1993)
MinError	Kittler and Illingworth, (1996)
Minimum	Prewitt and Mendelsohn, (1966)
Moments	Tsai (1985)
Otsu	Otsu (1979)
Percentile	Doyle (1962)
RenyiEntropy	Kapur et al., (1985)
Shanbhag	Shanbhag (1994)
Triangle	Zack et al., (1977)
Yen	Yen et al., (1995)

634

635

636 Table 3. Shrinkage area (S) and its relative error for selected functions (calibration image
 637 n°1)

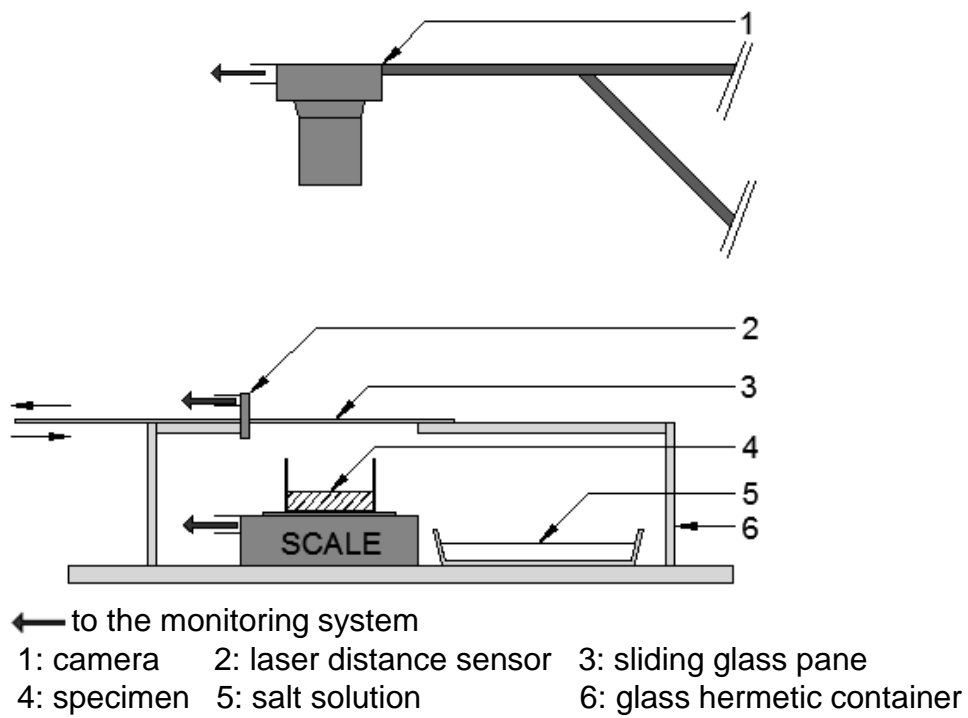
Threshold	S <i>px</i>	Relative Error %
MaxEntropy	142284	5.07
Otsu	155008	3.42
Huang	239355	59.69
Intermodes	23087	84.60
IsoData	152644	1.84
IJ_IsoData	141135	5.84
Mean	218104	45.51
Minimum	97845	34.72
Moments	158675	5.86
Percentile	254101	69.53
RenyiEntropy	142284	5.07
Triangle	247344	65.02
Yen	142284	5.07

638

639 Table 4. Result of relative error of shrinkage area according to the used threshold algorithm
 640 for the image of calibration n°2

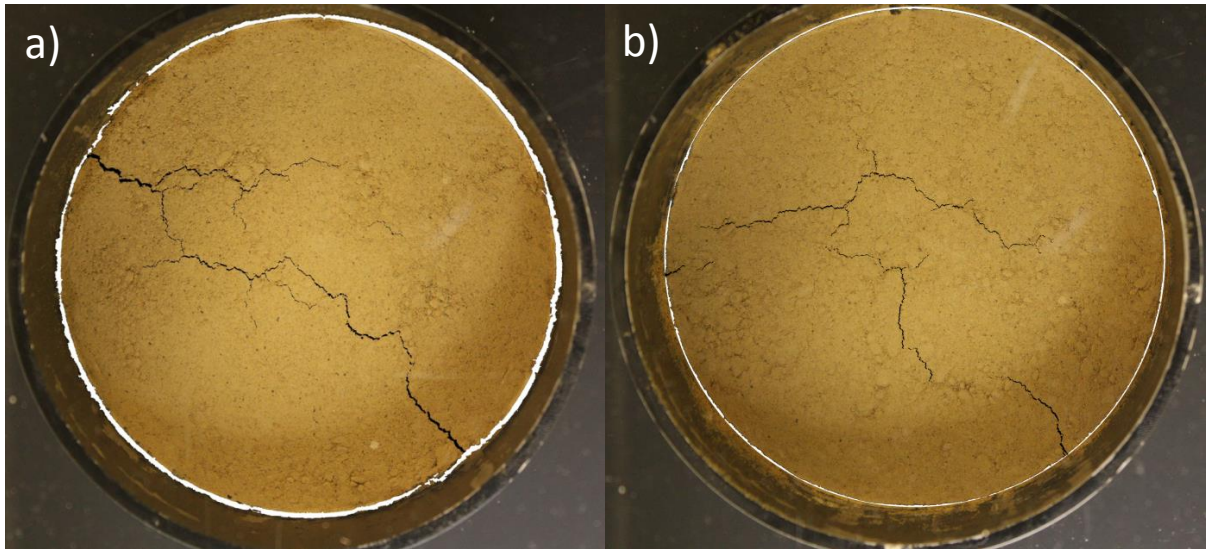
Threshold	S <i>px</i>	Relative Error %
MaxEntropy	49 166	2.60
Otsu	77 086	52.71
IsoData	69 387	37.47
IJ_IsoData	58 989	16.87
Moments	66 819	32.38
RenyiEntropy	48 185	4.54
Yen	49166	2.60

641



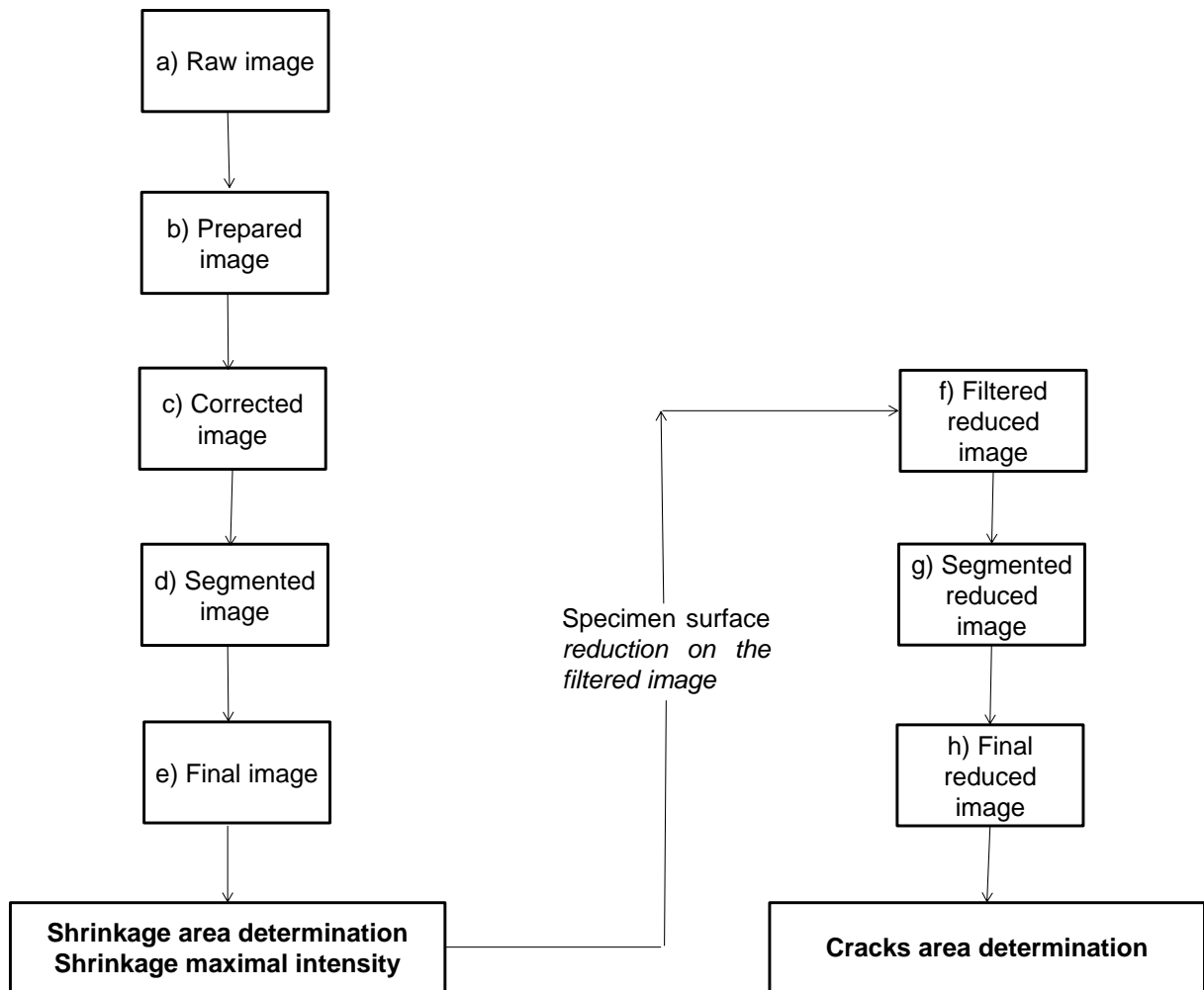
642

643 Fig.1. Schema of the experimental device



644

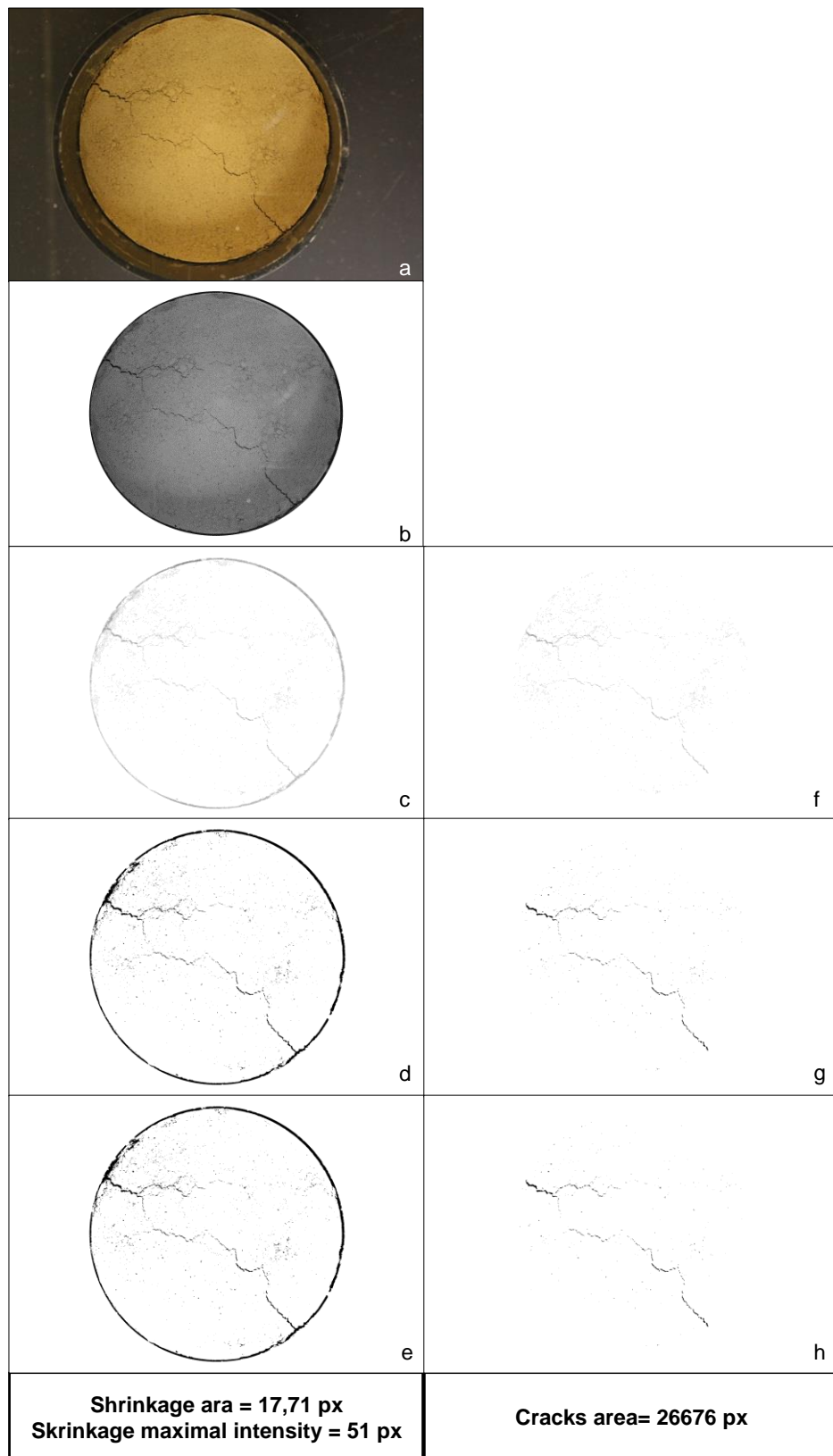
645 Fig. 2: Image of calibration n°1 after manual determination of the shrinkage area and the
 646 crack area (a) and image of calibration n°2 after manual determination of the shrinkage area
 647 and the crack area (b)



648

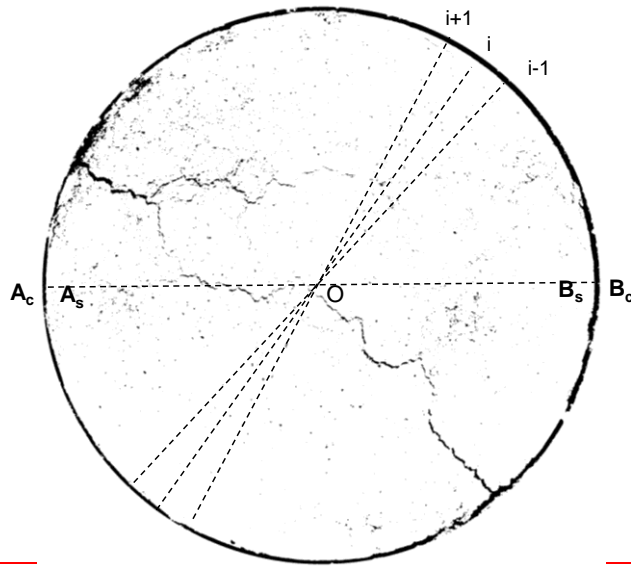
649 Fig.3. Chart of the image processing method

650



652

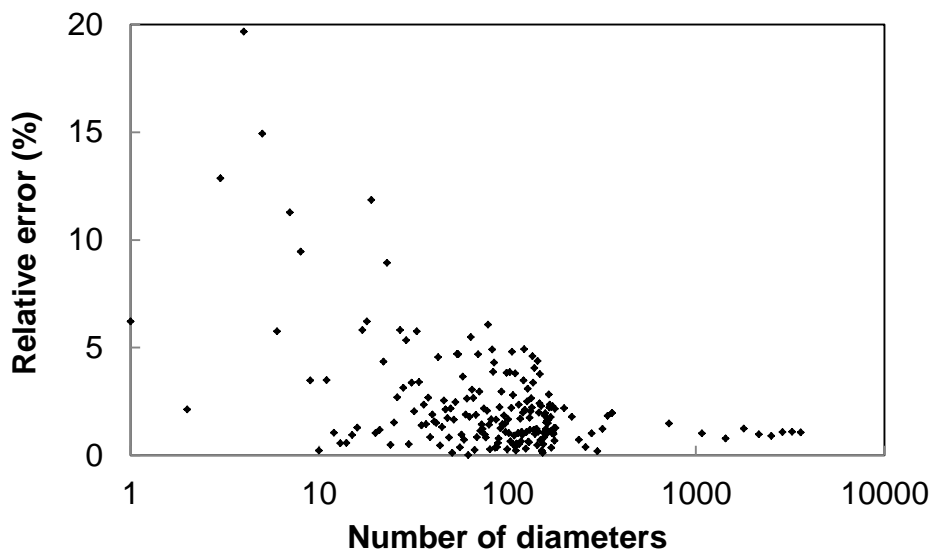
653 Fig.4. The different stages of the image processing method applied to the calibration image
 654 n°1: a) raw image b) prepared image, c) **corrected image** d) segmented image e) final image
 655 f) reduced **corrected image** g) segmented reduced image h) final reduced image



656

657 Fig.5. Diameter algorithm illustration for the given diameter of the final image of calibration

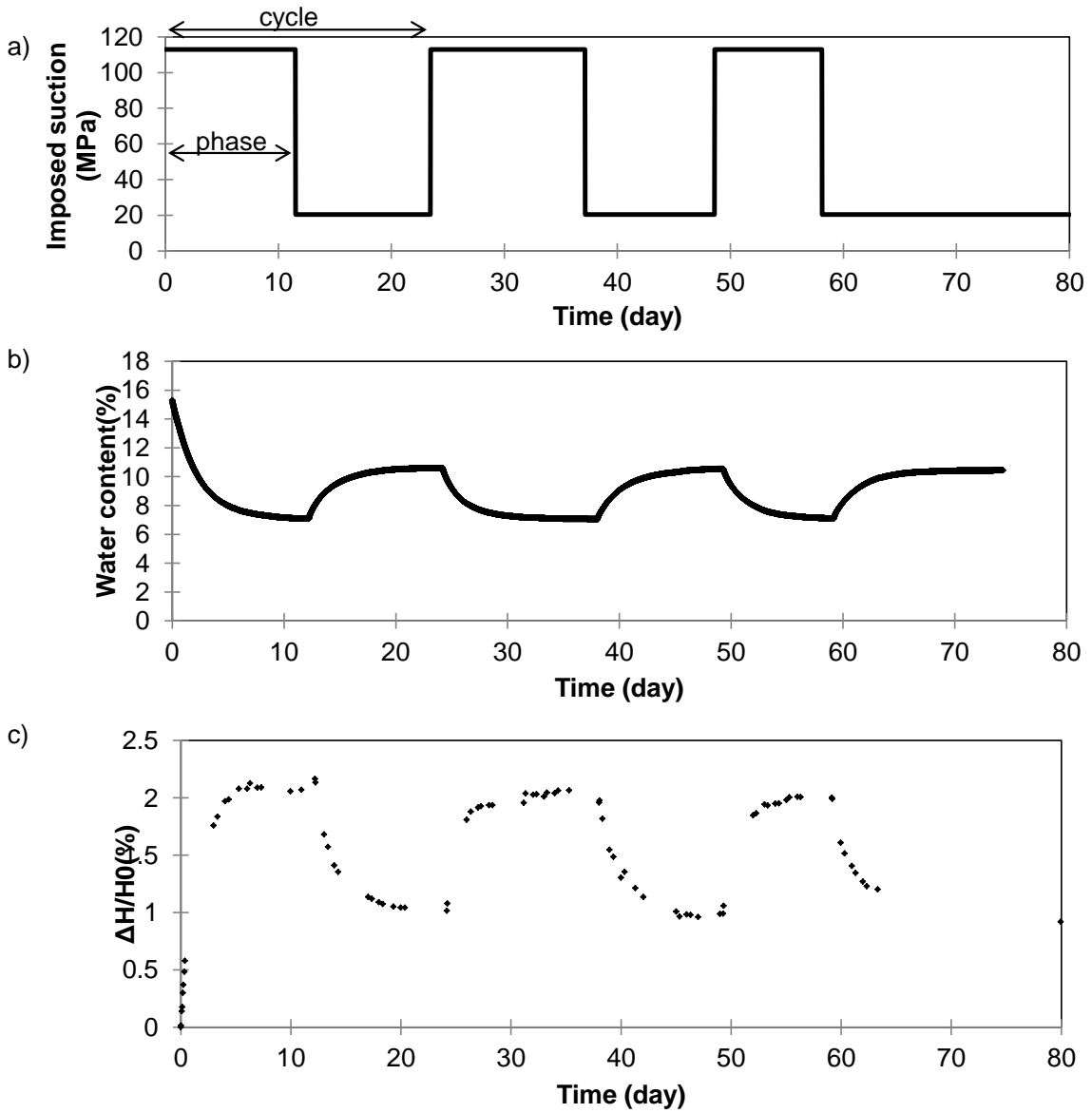
658



659

660 Fig.6. Impact of the number of diameters considered in the diameter algorithm on the relative
661 error of the shrinkage area prediction for the image of calibration

662

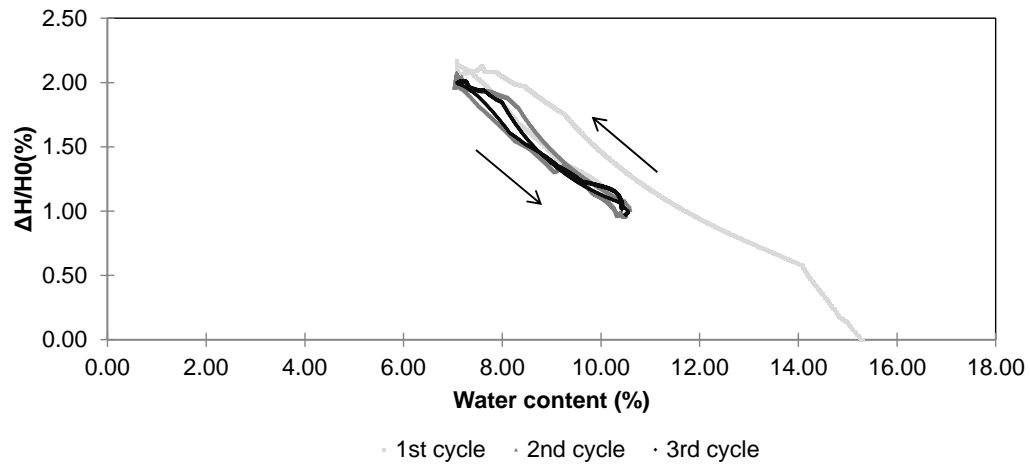


663

664 Fig.7. Evolution of the measured parameters over time during the test: a) The imposed
 665 suction, b) The specimen water content, c) The vertical shrinkage

666

667

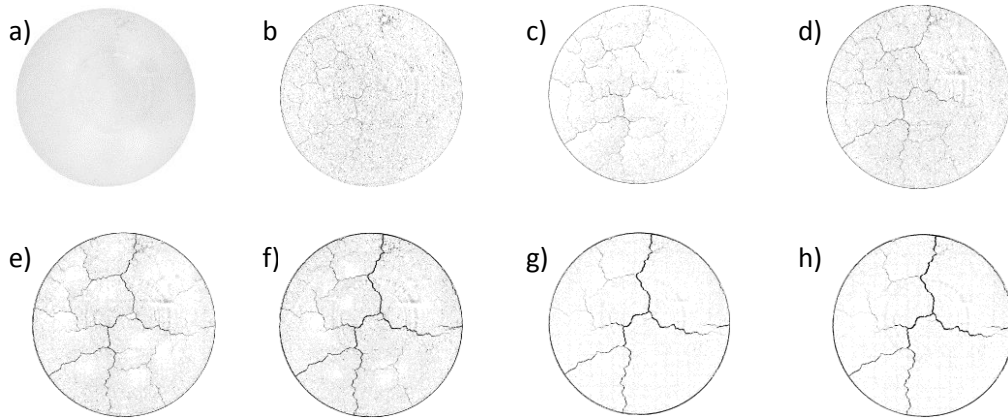


668

669

Fig.8. Evolution of the vertical strains with water content

670



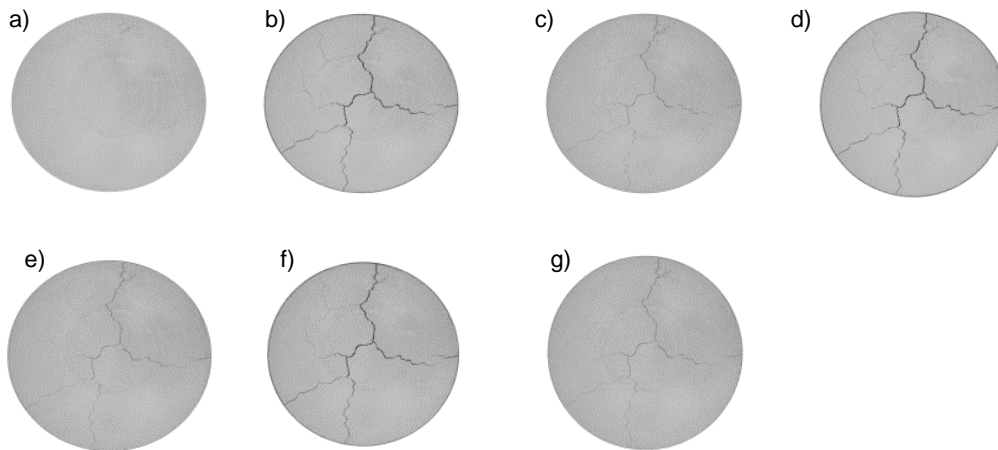
671

672 Fig.9. Evolution of the crack surface during the first phase of drying. a) Initial state*, b) after 4
673 h*, c) after 6 h*, d) after 10 h*, e) after 20 h*, f) after 44 h*, g) after 5 days*, h) after 11.5
674 days*

675

*: the contrast of these images was increased to improve the specimen cracks observation in this figure.

676



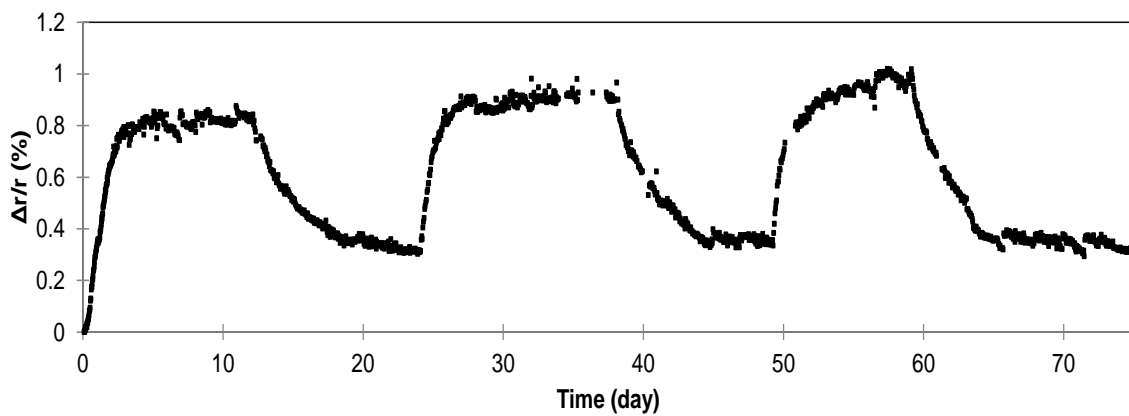
677

678 Fig. 10: Specimen surface at the different drying/wetting phase: a) initial state b) after the first
 679 drying phase c) after the first wetting phase d) after the second drying phase e) after the
 680 second wetting phase f) after the third drying phase f) after the third wetting phase.

681

682

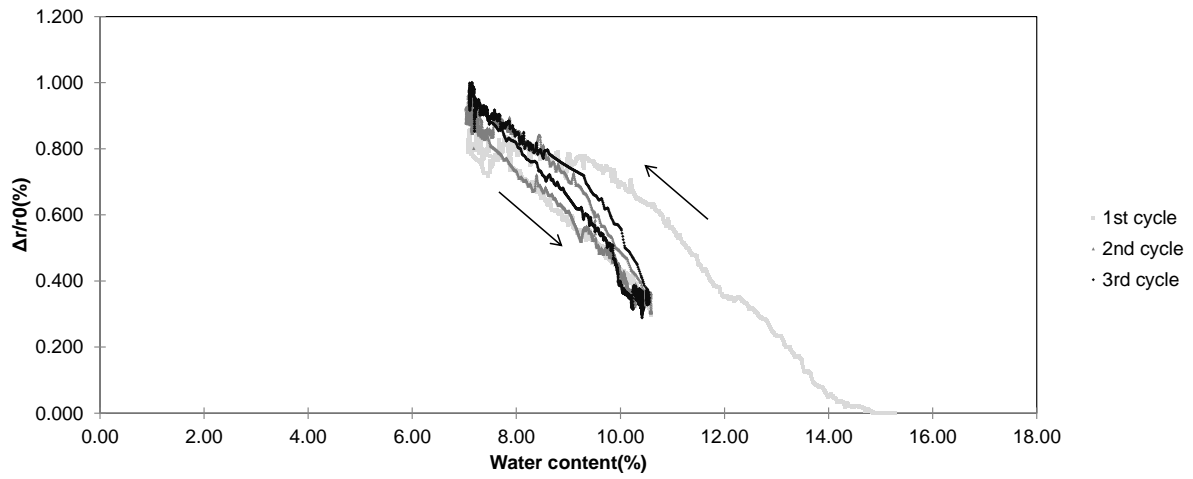
683



684

685 Fig.11. Evolution of horizontal strains over time

686



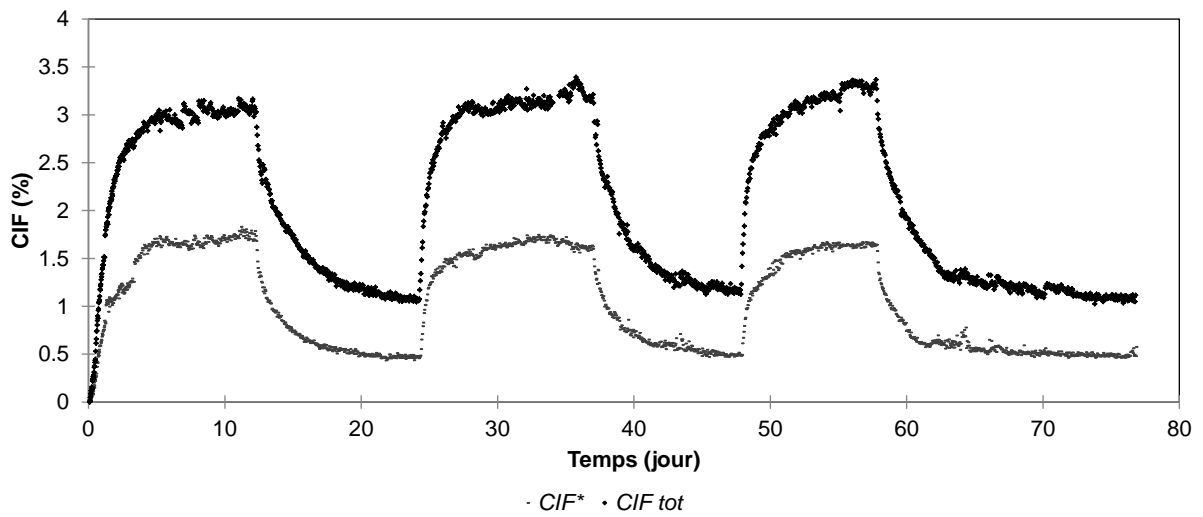
687

688 Fig.12. Evolution of radial strain with water content

689

690

691

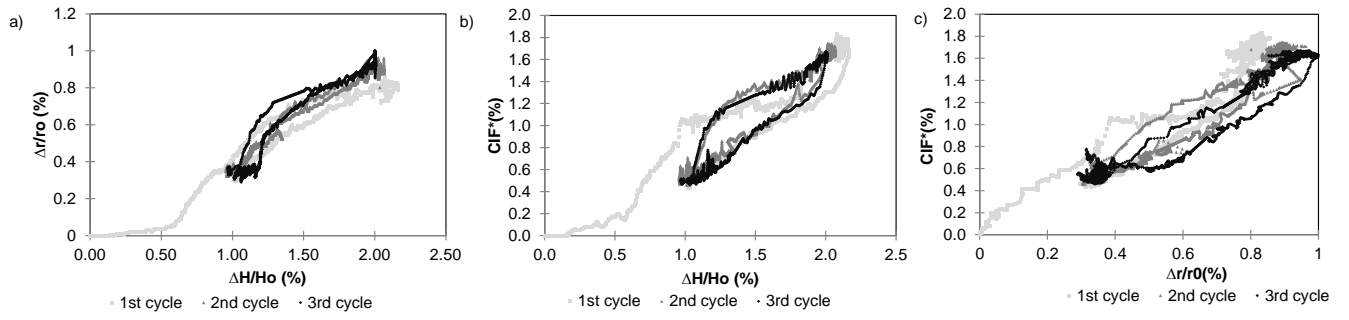


692

693 Fig.13. Evolution of the CIF^* and CIF_{tot} over time

694

695

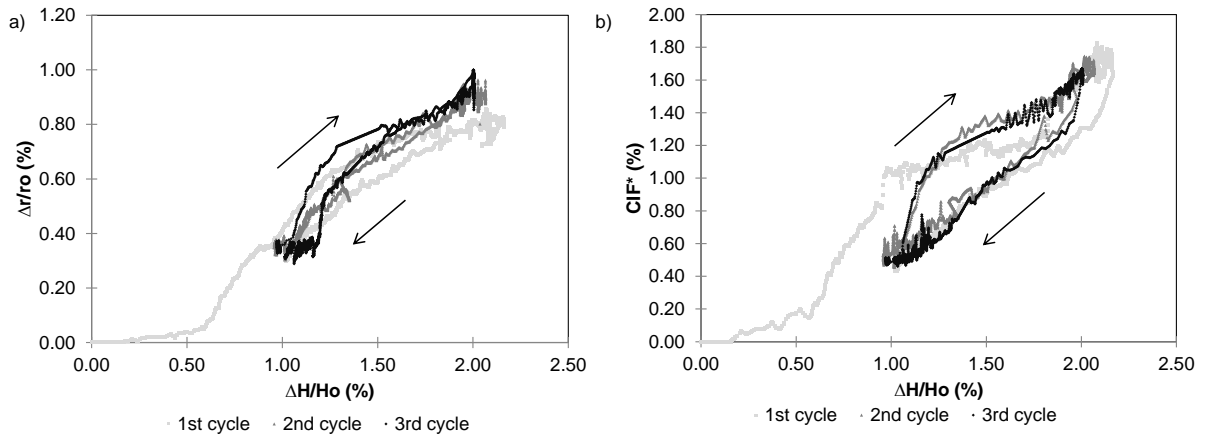


696

697 **Figure 14: Evolution of measured parameters a) The radial strains with the vertical strains b)**

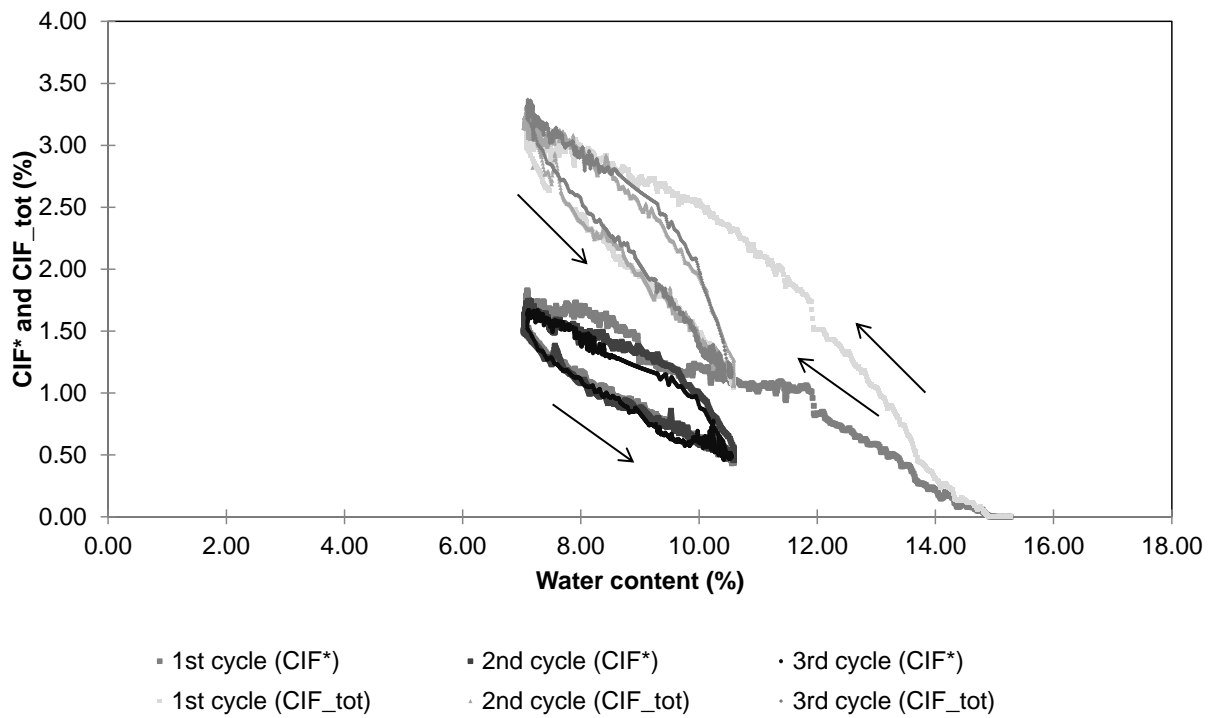
698 **CIF^* with vertical strains c) CIF^* with radial strains**

699



700

701 Fig.14. Evolution of the measured parameters with $\Delta H/H_o$, a) radial strains, b) CIF^*



702

703 Fig.15. Comparison between the CIF_{tot} and CIF^*

704

705

706